Improved description of the potential energy surface in BaTiO3 by anharmonic phonon coupling

Florian Mayer, Maxim N. Popov, Donald M. Evans, Stephan Krohns, Marco Deluca, Jürgen Spitaler

Angaben zur Veröffentlichung / Publication details:

Mayer, Florian, Maxim N. Popov, Donald M. Evans, Stephan Krohns, Marco Deluca, and Jürgen Spitaler. 2022. "Improved description of the potential energy surface in BaTiO3 by anharmonic phonon coupling." *Physical Review B* 106 (6): 064108. https://doi.org/10.1103/physrevb.106.064108.

Improved description of the potential energy surface in $BaTiO_3$ by anharmonic phonon coupling

Florian Mayer,[1,*] Maxim N. Popov,[1] Donald M. Evans,[2] Stephan Krohns,[2] Marco Deluca,[1] and Jürgen Spitaler[1]
[1]*Materials Center Leoben Forschung GmbH, Roseggerstrasse 12, 8700 Leoben, Austria*
[2]*Experimental Physics V, Center for Electronic Correlations and Magnetism, Institute of Physics, University of Augsburg, 86135 Augsburg, Germany*

(Received 9 March 2022; revised 13 June 2022; accepted 8 August 2022; published 22 August 2022)

Barium titanate (BT) based materials are at the forefront of materials being searched as possible candidates for the replacement of lead-based compositions in applications ranging from piezoelectrics to energy storage devices. Computational methods are very promising to increase the efficiency of materials discovery, provided that finite temperature properties can be realistically computed using, for example, molecular dynamics (MD). In this work, we present a systematic increase of the quality of MD simulations via an alternative way to calculate anharmonic contributions to the potential energy surface (PES) of barium titanate. A large number of first-principles calculations are performed, which are subsequently used to parametrize an effective Hamiltonian. To test the effects on various physical properties, MD simulations for the determination of transition temperatures, hysteresis, and permittivity of BT are shown. Furthermore, measurements were performed on BT single crystals to compare them directly with the MD simulations. It is observed that by incorporating a large number of anharmonic couplings, the description of the local minima in the PES becomes more accurate than in previous simulations. This leads to a better prediction of phase transition temperatures and shows the importance of anharmonic couplings in barium titanate. The presented approach can be directly adapted for other perovskite structures.

DOI: 10.1103/PhysRevB.106.064108

I. INTRODUCTION

An ever-growing demand for environmentally friendly materials is impacting the microelectronics industry. Many devices where ferroelectric materials are currently used are primarily based on environmentally critical lead-containing materials. In particular, the application of ferroelectrics as piezoelectric actuators [1] and as capacitive energy storage devices [2] has received renewed attention in recent years. Therefore, while it is of great importance to search for new alternative ferroelectric materials, there is also a need to understand the fundamental properties of established materials to provide clear goals for this search. Important parameters that need to be optimized in lead-free ferroelectrics are, for instance, piezoelectric coefficients, piezoelectric coupling factors, dielectric permittivity, and recoverable energy density. The compositional search space for lead-free perovskites is very large [3–5]; hence computational data-driven or even artificial intelligence (AI) methods are needed to improve the efficiency of materials discovery and accelerate experimental procedures [6], which are often based on trial and error. To enable such computational methodologies in the absence, or scarcity, of experimental data, it is necessary to calculate material properties at finite temperatures based on supercells consisting of millions of atoms—in order to reproduce both short-range and long-range order. Such molecular dynamics (MD) simulations rely on approaches derived from density functional theory (DFT) involving, for example, effective Hamiltonians [7–9], which thus need to be developed case by case for different compositions.

In this work, we address the effective Hamiltonian approach taking pure barium titanate [$BaTiO_3$ (BT)] as an example of a lead-free perovskite material. BT is considered as the prototypical ferroelectric material, and many of its chemical modifications have demonstrated excellent performance in piezoelectric [10], energy storage [11], microwave [12], and electrocaloric [13] applications. BT itself is already quite a complex material. It shows four different phases, three of which (rhombohedral, orthorhombic, and tetragonal) are ferroelectric, whereas the high-temperature cubic phase is paraelectric. The corresponding phase transitions make this material and its modifications interesting for many applications since excellent properties such as giant dielectric permittivity and large piezoelectric coefficients, driven by a large spontaneous polarization, can be observed close to these phase transitions [14]. Various methods have been used to explain the origins [15] of ferroelectric behavior in BT. The primary examples of this are first- principles calculations based on density functional theory (DFT) [16–19], semiempirical methods [20], and phase-field approaches [21,22]. Devonshire was one of the first to study the origin of ferroelectricity in BT using Landau-Devonshire theory [23,24]. In the 1990s, Cohen and Krakauer [17] showed the now well-known double well shaped energy surface of BT calculated using DFT. This was followed by the development of semiempirical models, which are still used in the simulation of BT. Of particular note is the work of Zhong *et al.* [18] in developing effective Hamiltonians to simulate properties at finite temperatures. The basic idea was to reduce the complexity and describe the potential energy surface as a function of a small number of variables [25], where first-principles calculations can determine the required parameters. In the early stages, this approach was a mean-field theory which was later adapted to

*florian.mayer@mcl.at

a local-mode theory [26] allowing simulations of supercells. Furthermore, this approach has been continuously extended to investigate doped systems as well [7–9]. In 2008, Nishimatsu *et al.* [27] revised this concept by giving a makeover to the formalism, thereby increasing efficiency and accuracy.

In 2017, Paul *et al.* [28] showed that the extension of the self-energy by contributions from anharmonic couplings to higher-energy phonon modes gives an improved description of the potential energy surface. Since the original formalism is parametrized exclusively by the soft mode and its displacement pattern, the extension by including further phonon modes offers an interesting possibility to increase the accuracy of the effective Hamiltonian.

In this paper we introduce a revised effective Hamiltonian which is based on a larger number of anharmonic terms which, therefore, yield a better description of the potential energy surface. Furthermore, we present a systematic way of deriving these anharmonic couplings from first- principles calculations. To test our revised model, we have carried out various measurements on BT single crystals and compared them with predictions from our simulations. The focus of this benchmark is on dielectric properties such as permittivity and hysteresis curves.

This paper is organized as follows: In Sec. II, a revised scheme for including anharmonic couplings for the self-energy in the effective Hamiltonian approach is derived. Building on this, in Sec. III, we show the parametrization by first-principles calculations. Finally, Sec. IV uses our parameter set for MD simulations and compares it to experimental measurements on BT single crystals.

II. THEORETICAL FRAMEWORK

A. Definition of local-mode self-energy

In 2008, Nishimatsu *et al.* [27] presented a revised effective Hamiltonian, which has the following form:

$$H^{\text{eff}} = \frac{M^*_{\text{dipole}}}{2}\sum_{\boldsymbol{R},\alpha}\dot{u}^2_\alpha(\boldsymbol{R}) + \frac{M^*_{\text{acoustic}}}{2}\sum_{\boldsymbol{R},\alpha}\dot{w}^2_\alpha(\boldsymbol{R}) + V^{\text{self}}(\{\boldsymbol{u}\}) + V^{dpl}(\{\boldsymbol{u}\}) + V^{\text{short}}(\{\boldsymbol{u}\}) + V^{\text{elas,homo}}(\eta_1,\ldots,\eta_6) + V^{\text{elas,inho}}(\{\boldsymbol{w}\}) + V^{\text{coupl,homo}}(\{\boldsymbol{u}\},\eta_1,\ldots,\eta_6) + V^{\text{coupl,inho}}(\{\boldsymbol{u}\},\{\boldsymbol{w}\}) - Z^*\sum_R \epsilon\cdot u(\boldsymbol{R}). \quad (1)$$

The Hamiltonian is a function of variables $\{\boldsymbol{u}\}$, the amplitude of the optical soft mode, where the brackets $\{\cdots\}$ represent a set of amplitudes in a supercell. Further variables within the Hamiltonian are dimensionless displacement vectors $\boldsymbol{w}$ for each unit cell and strain variables η_l in Voigt notation. M^*_{dipole} and M^*_{acoustic} represent effective masses of $\boldsymbol{u}$ and $\boldsymbol{w}$, respectively. $\boldsymbol{R}$ is the position of a unit cell within the supercell. Z^* is the Born effective charge corresponding to the soft mode and ϵ represents an external field. The time derivatives of the variables are given by $\dot{u}_\alpha$ and $\dot{w}_\alpha$, where α denotes the Cartesian component. The total energy comprises five potential energy contributions: a local-mode self-energy V^{self}, the dipole-dipole interaction V^{dpl}, the short-range interaction V^{short}, the homogeneous and inhomogeneous contributions of the elastic energy ($V^{\text{elas,homo}}$ and $V^{\text{elas,inho}}$, respectively), and the homogeneous and inhomogeneous contributions of the strain-phonon coupling ($V^{\text{coupl,homo}}$ and $V^{\text{coupl,inho}}$, respectively). For enabling MD simulations, the kinetic energies of the optical soft mode and the long-wavelength limit of the acoustic branch [first and second terms on the right-hand side of Eq. (1)] are considered. The last term in Eq. (1) allows applying external fields to the supercell. A more detailed description of all terms can be found in Ref. [27].

To derive a scheme for including anharmonic couplings to higher-energy phonons, we first shortly recap the definition of the local-mode self-energy as found in the literature [29]. The original mathematical expression defined by King-Smith *et al.* [25] was given by a fourth-order polynomial of the soft-mode amplitude vector $\boldsymbol{u}$. Nishimatsu *et al.* [29] extended this expression up to the eighth order for a more accurate description of anharmonic contributions originating from $\boldsymbol{u}$. The complete term for the self-energy defined by Nishimatsu *et al.* [29] is presented in Eq. (2), where κ_2, α, γ, k_1, k_2, k_3, and k_4 represent parameters. The sum over $\boldsymbol{R}$ accounts for each unit cell in the supercell.

$$V^{\text{self}}(\{\text{u}\}) = \sum_R \Big\{\kappa_2 u^2(\boldsymbol{R}) + \alpha u^4(\boldsymbol{R}) + \gamma\big[u_y^2(\boldsymbol{R})u_z^2(\boldsymbol{R}) + u_z^2(\boldsymbol{R})u_x^2(\boldsymbol{R}) + u_x^2(\boldsymbol{R})u_y^2(\boldsymbol{R})\big] + k_1 u^6(\boldsymbol{R}) + k_2\big(u_x^4(\boldsymbol{R})*\big[u_y^2(\boldsymbol{R}) + u_z^2(\boldsymbol{R})\big] + u_y^4(\boldsymbol{R})*\big[u_z^2(\boldsymbol{R}) + u_x^2(\boldsymbol{R})\big] + u_z^4(\boldsymbol{R})*\big[u_x^2(\boldsymbol{R}) + u_y^2(\boldsymbol{R})\big]\big) + k_3 u_x^2(\boldsymbol{R})u_y^2(\boldsymbol{R})u_z^2(\boldsymbol{R}) + k_4 u^8(\boldsymbol{R})\Big\}. \quad (2)$$

In further sequence, we evaluate the above equation for a single unit cell in the high-symmetry directions ⟨001⟩, ⟨011⟩, and ⟨111⟩. We denote the resulting self-energies as $E(u)$, and obtain them by substituting the expressions $\boldsymbol{u} = (0,0,u)$, $\boldsymbol{u} = (0,u,u)$, and $\boldsymbol{u} = (u,u,u)$, respectively, for the soft-mode amplitude. That results in Eqs. (2a)–(2c) and will also be used for the parametrization in Sec. II C:

$$E_{001}(u) = \kappa u^2 + \alpha u^4 + k_1 u^6 + k_4 u^8, \quad (2a)$$

$$E_{011}(u) = \kappa u^2 + \left(\alpha + \tfrac{1}{4}\gamma\right)u^4 + \left(k_1 + \tfrac{1}{4}k_2\right)u^6 + k_4 u^8, \quad (2b)$$

$$E_{111}(u) = \kappa u^2 + \left(\alpha + \tfrac{1}{3}\gamma\right)u^4 + \left(k_1 + \tfrac{2}{9}k_2 + \tfrac{1}{27}k_3\right)u^6 + k_4 u^8. \quad (2c)$$

This energy contribution arises from local displacements according to the displacement pattern of the soft mode. The interaction with neighboring unit cells as well as the energy contribution of associated elastic effects is not included here. The latter are accounted for by strain-phonon coupling and various elastic terms in the Hamiltonian as described above.

B. Scheme for including anharmonic couplings

In this section, we derive a revised scheme for including anharmonic couplings to higher-energy phonons within the local-mode self-energy. For the construction of the effective Hamiltonian presented in Eq. (1), the choice of a local basis by lattice Wannier functions (LWFs) is required [30,31]. However, this choice is not unambiguous and should be carried out under the following aspects. For cubic BT, the highest symmetry can be obtained by the choice of LWFs centered on the A site or B site. Since it is mainly the B site that is responsible [31] for the ferroelectric distortions, it is advantageous to define it as the center of the LWFs. For the remainder of this paper, we will use this B-centered basis for all derivations and calculations including all phonon modes. As a next step, we have to define the phonon modes which are serving as the basis in the conventional effective Hamiltonian of Eq. (1). In cubic BT, there are five eigenmodes with each of them being triply degenerate. Besides the acoustic mode, there are three optical modes with Γ_{15} symmetry and one optical mode with Γ_{25} symmetry [25,28,30]. Of particular interest are the optical Γ_{15} eigenmodes, which are responsible for the ferroelectric transition [25]. We will refer to them as u (soft mode, imaginary frequency of $193i\,\mathrm{cm}^{-1}$), v_1 ($178\,\mathrm{cm}^{-1}$), and v_2 ($468\,\mathrm{cm}^{-1}$). The corresponding eigenvectors and frequencies can be calculated by means of DFT. For details we refer to the next section. The eigenvector components of the interatomic force constant (IFC) matrix for the soft mode are estimated with values of $\xi_{\mathrm{Ba}} = 0.157$, $\xi_{\mathrm{Ti}} = 0.774$, $\xi_{\mathrm{O1,O2}} = -0.195$ and $\xi_{\mathrm{O3}} = -0.547$. Here, we listed barium, titanium, and oxygen values in the five-atom unit cell, whereby O_1 and O_2 denote the oxygens in plane with the titanium atom. Analogously the patterns for v_1 and v_2 can be calculated: $\xi^{v_1}_{\mathrm{Ba}} = 0.862$, $\xi^{v_1}_{\mathrm{Ti}} = -0.311$, $\xi^{v_1}_{\mathrm{O1,O2}} = -0.281$, $\xi^{v_1}_{\mathrm{O3}} = 0.010$, and $\xi^{v_2}_{\mathrm{Ba}} = -0.172$, $\xi^{v_2}_{\mathrm{Ti}} = 0.317$, $\xi^{v_2}_{\mathrm{O1,O2}} = -0.427$, $\xi^{v_2}_{\mathrm{O3}} = 0.709$. To obtain the contributions of these phonons to the ferroelectric distortion between cubic and tetragonal phase, we started with calculating the associated displacement pattern $\vec{f}$. The components of the pattern result in $f_{\mathrm{Ba}} = 0.114$ Å, $f_{\mathrm{Ti}} = 0.219$ Å, $f_{\mathrm{O1,O2}} = -0.079$ Å, and $f_{\mathrm{O3}} = -0.007$ Å. Comparing the ferroelectric distortion with the soft-mode pattern shows a large overlap. Owing to that, the main part of the ferroelectric distortion can be described by the soft mode and, therefore, this mode is chosen as the basis for the effective Hamiltonian in Eq. (1). The acoustic mode is also included by the variables w within the long-wavelength limit. The other phonons have not been considered so far. However, Paul *et al.* [28] showed in their work that not only the soft mode u, but also the coupling with the modes v_1 and v_2 have an influence on the phase transitions. To quantify this contribution, we will apply the same approach as suggested by Paul *et al.* [28]. That is, we use the equation $\vec{S} = \vec{f} - (\vec{f}\cdot\hat{e}_{\mathrm{soft}})\hat{e}_{\mathrm{soft}}$, where $\vec{S}$ is the fraction of the displacement not yet covered by the soft mode. $\hat{e}_{\mathrm{soft}}$ represents the soft-mode eigenvector and $\vec{f}$ the ferroelectric distortion from above. Thus, the overlap of $\vec{S}$ with the phonon modes not yet considered in the effective Hamiltonian can now be calculated. The determined overlap of v_1 can be quantified as 0.85 and that of v_2 as 0.26. In contrast, the Γ_{25} mode shows a negligible overlap. Due to that, for an improved description of the potential energy surface, the inclusion of v_1 and v_2 is relevant. The next step is to lay the mathematical foundation for this inclusion. To account for the contributions of these high-energy modes, Paul *et al.* [28] developed the self-energy as a Taylor series in eighth order of u and second order of v_1 and v_2, where mixed terms between u and either v_1 or v_2 were considered. Since we cannot make *a priori* statements about the importance of individual couplings we decided to take a more general approach. Therefore, we start with the extension of the self-energy by an approximation by means of a multivariate Taylor series as written in Eq. (3). In this paper, we deal exclusively with the ⟨001⟩ direction. A possible involvement of the other directions will be discussed further below. The variables Taylor series are the amplitudes of the phonon modes u, v_1, and v_2. The evaluation of the series is done around the cubic phase. Therefore, we set $u_0 = 0$, $v_{1,0} = 0$ and $v_{2,0} = 0$. For the soft-mode amplitude u, we expand the series up to the eighth order ($n_1 = 0, \ldots, 8$):

$$E^{\mathrm{anh}}_{001}(u, v_1, v_2) = \sum_{n_1}^{8}\sum_{n_2}^{6}\sum_{n_3}^{6} \frac{(u-u_0)^{n_1}(v_1-v_{1,0})^{n_2}(v_2-v_{2,0})^{n_3}}{n_1!n_2!n_3!}\left(\frac{\partial^{n_1+n_2+n_3}E(u,v_1,v_2)}{\partial u^{n_1}\partial v_1^{n_2}\partial v_2^{n_3}}\right)(u_0, v_{1,0}, v_{2,0}). \tag{3}$$

In contrast to Paul *et al.* [28], the series expansion is also performed for v_1 and v_2 up to the sixth order ($n_{2,3} = 0, \ldots, 6$). The series expansion in full form can be found in the Supplemental Material [32] in Eq. (S1). Due to the symmetry of the cubic phase, various couplings are zero by definition. These can be determined, for example, by the program ISOTROPY [33,34]. The latter was used to rewrite the full-form function from Eq. (S1) [32]. Thus, the forbidden couplings were removed and the remaining ones were replaced by parameters a_i, b_i, c_i, and d_i. The resulting function for the self-energy in the ⟨001⟩ direction is written in Eq. (4). The parameters c_i are analogous to those used in Eq. (2a). The parameters a_i and b_i, which represent couplings between u and either v_1 or v_2, are introduced. The parameters d_i are mixed couplings of u, v_1, and v_2.

$$\begin{aligned}E_{001}(u, v_1, v_2) = {} & c_0 + c_1u^2 + c_2u^4 + c_3u^6 + c_4u^8 + a_1uv_1 + a_2v_1^2 + a_3u^3v_1 + a_4u^2v_1^2 + a_5uv_1^3 + a_6v_1^4 + a_7u^5v_1 + a_8u^4v_1^2 \\ & + a_9u^3v_1^3 + a_{10}u^2v_1^4 + a_{11}uv_1^5 + a_{12}v_1^6 + b_1uv_2 + b_2v_2^2 + b_3u^3v_2 + b_4u^2v_2^2 + b_5uv_2^3 + b_6v_2^4 + b_7u^5v_2 \\ & + b_8u^4v_2^2 + b_9u^3v_2^3 + b_{10}u^2v_2^4 + b_{11}uv_2^5 + b_{12}v_2^6 + d_1v_1v_2 + d_2u^2v_1v_2 + d_3uv_1^2v_2 + d_4uv_1v_2^2 + d_5v_1^3v_2 \\ & + d_6v_1^2v_2^2 + d_7v_1v_2^3 + d_8u^4v_1v_2 + d_9u^3v_1^2v_2 + d_{10}u^3v_1v_2^3 + d_{11}u^2v_1^3v_2 + d_{12}u^2v_1^2v_2^2 + d_{13}u^2v_1v_2^3 + d_{14}uv_1^4v_2 \\ & + d_{15}uv_1^3v_2^2 + d_{16}uv_1^2v_2^3 + d_{17}uv_1v_2^4 + d_{18}v_1^5v_2 + d_{19}v_1^4v_2^2 + d_{20}v_1^3v_2^3 + d_{21}v_1^2v_2^4 + d_{22}v_1v_2^5.\end{aligned} \tag{4}$$

The derived equation contains many anharmonic couplings, so that a direct determination of the necessary parameters as shown in Paul *et al.* [28] is no longer possible. To determine all couplings as accurately as possible, an alternative approach involving the fitting of anharmonic couplings [35] will be used in Sec II D. For now, let us assume that we have already determined all the coupling parameters. That means we now have a function for the local-mode self-energy, which depends on u, v_1, and v_2, and is not compatible with the effective Hamiltonian defined in Eq. (1). A solution to this issue would be to extend the whole Hamiltonian by these additional degrees of freedom, but that would be beyond the scope of this paper. In fact, a significant advantage of the effective Hamiltonian lies in its computational speed, and adding more degrees of freedom would change that. To recast our expansion in Eq. (3) to a function of one variable, we can compute the amplitudes v_1 and v_2 that minimize [28] the self-energy for any value of u. Unfortunately, an analytical solution is not feasible in our case due to the complexity of Eq. (3). Therefore, we decided to use a numerical optimization scheme to search for the minimizing $v_{1,\min}(u_i)$ and $v_{2,\min}(u_i)$ amplitudes corresponding to a given discrete value of u_i. This allows us to compute the minimum self-energy as a function of u for a chosen discrete range, as shown schematically in this equation:

$$E_{001}(u_i) = E_{001}^{\text{anh}}[u_i, v_{1,\min}(u_i), v_{2,\min}(u_i)]. \tag{5}$$

As the method for the minimization of v_1 and v_2 we used the Nelder-Mead algorithm [36] for two dimensions.

Finally, for the effective Hamiltonian, we again need an analytic function for the self-energy. The simplest solution is to take Eq. (2a) and fit the data, which now include contributions from anharmonic couplings. This approach is similar to the approximation in Paul *et al.* [28], where they insert their additional anharmonic contribution into the parameters k_1 and k_4.

An advantage of the above-derived scheme for including anharmonic couplings is that it can be used analogously for the other directions ⟨011⟩ and ⟨111⟩. The only difference lies in estimating the coupling parameters via fitting, which will be discussed in detail in the next section.

C. Parameters of conventional Hamiltonian

In this section we briefly discuss the parametrization of the conventional effective Hamiltonian, i.e., the one defined by Nishimatsu *et al.* [29]. However, we will refrain from a detailed description of all energy terms to be parametrized since this has already been discussed sufficiently in other publications [25,28,29]. Since we use the PBEsol functional [37] in contrast to other parametrizations in the literature, we will nevertheless give an overview of the differences and similarities. A detailed description of the DFT settings and a comparison of the obtained parameters with other exchange-correlation functionals [38,39] are provided in the Supplemental Material [32]. In general, parametrization starts with the relaxation of the cubic phase. In our case, this resulted in a lattice constant of $a_0 = 3.987$ Å, which agrees very well with other PBEsol results from the literature [20,40]. Compared to the value obtained with the Wu-Cohen functional [29,41] of $a_{\text{WC}} = 3.986$ Å, the PBEsol yields an almost identical value. Also the SCAN (Strongly-constrained and appropriately-normed) functional [42] yields a very similar value [28] of $a_{\text{SCAN}} = 3.99$ Å. Altogether, all three functionals yield results close to the experimental value [25] of $a_{\text{expt}} = 4.01$ Å.

The next step is to calculate the eigendisplacements, which are the eigenvectors of the second-order force constant matrix. The latter was calculated using the frozen-phonon method implemented within the VASP package (IBRION 5 tag). To check the obtained results, we also carried out a density functional perturbation theory (DFPT) calculation using the IBRION 7 tag within VASP. Both approaches agree well with each other and yield eigenvector components as listed in the previous section. We now take this soft-mode displacement pattern as the basis for the effective Hamiltonian. To parametrize the local-mode self-energy, we displace the atoms in the different directions, ⟨001⟩, ⟨011⟩, and ⟨111⟩, using the soft-mode pattern. Then Eqs. (2a)–(2c) are used to determine the parameters κ, α, γ and k_1–k_4 by fitting. An overview of the obtained values can be found in Table I. Since these parameters strongly depend on the chosen order of the polynomial and on the chosen exchange-correlation functional, we refrain here from a comparison with values from the literature. Another energy contribution represents the coupling of phonons with the deformation of the unit cell. The parametrization for this case was performed in two different ways. The first method adheres to the literature [25]; i.e., atomic displacements according to the soft mode were frozen in, and the shape of the unit cell was varied. That allows the calculation of the change in the harmonic coefficient κ as a function of strain η, which in turn allows the coupling parameters to be determined. As a second approach, we considered the following. We displaced the atoms analogously to the first approach, but then the internal coordinates were fixed and the unit cell shape and volume were relaxed for each displacement. VASP allows this through the setting ISIF 6. To extract the coupling parameters, we used the scheme Nishimatsu *et al.* used for their valley tracing method (VTM) [29]. The results of the two approaches vary slightly, with values of $B_{1xx} = -230.75$ eV/Å^2, $B_{1yy} = -21.76$ eV/Å^2, and $B_{4yz} = -15.56$ eV/Å^2 determined with the first approach. In contrast, the values of the second method are $B_{1xx} = -235.06$ eV/Å^2, $B_{1yy} = -19.34$ eV/Å^2, and $B_{4yz} = -15.33$ eV/Å^2. Since the second method optimizes each unit cell and allows a larger number of calculated displacements, these parameters are used for the rest of this paper. A more detailed description of each method can be found in the Supplemental Material [32]. Next, we turn to the determination of elastic constants. Since we use the cubic phase as a reference for the description of our system, the number of independent constants is reduced to three. These are given by B_{11}, B_{12}, and B_{44}, whereby these values are obtained from the elastic constants multiplied by the unit cell volume. The calculation was performed by applying different deformations [29] to the unit cell and fitting the equation of state. The corresponding results are listed in Table I.

The determination of short-range interaction parameters j_1–j_7 was done analogously to the procedure proposed by Nishimatsu *et al.*; that is, a series of phonon calculations at various high-symmetry points in reciprocal space was used

TABLE I. Parameters for the effective Hamiltonian describing pure BT.

Elastic and coupling		Self-energy		Short range and long range	
m^* (amu)	38.148	κ (eV/Å^2)	–1.965	Z^* (e)	10.267
B_{11} (eV)	126.137	κ_2 (eV/Å^2)	8.007	ε_∞	6.847
B_{12} (eV)	42.391	α (eV/Å^4)	123.492	j_1 (eV/Å^2)	–2.060
B_{44} (eV)	50.046	γ (eV/Å^4)	–165.344	j_2 (eV/Å^2)	–1.173
B_{1xx} (eV/Å^2)	–235.064	k_1 (eV/Å^6)	–528.388	j_3 (eV/Å^2)	0.680
B_{1yy} (eV/Å^2)	–19.341	k_2 (eV/Å^6)	123.688	j_4 (eV/Å^2)	–0.610
B_{4yz} (eV/Å^2)	–15.333	k_3 (eV/Å^6)	307.317	j_5 (eV/Å^2)	0.000
		k_4 (eV/Å^8)	3370.229	j_6 (eV/Å^2)	0.277
				j_7 (eV/Å^2)	0.000

to provide the necessary eigenvalues for the linear system of equations (see Eqs. (15a)–(15g) in Ref. [29]). By solving this system of equations, the parameters j_1–j_7 and κ_2 could be determined, which are listed in Table I. It should be noted that the κ_2 value was adapted according to Eq. (17) in Ref. [29]. The remaining parameters in Table I were derived from a DFPT calculation. Table I also includes the Born effective charge of the soft mode as well as the optical dielectric constant, obtained from DFPT. The effective mass m^* was calculated by using the soft-mode eigenvector and the corresponding atomic masses of the ions.

D. Fitting of anharmonic couplings

In Sec. II B, we discussed a scheme to include additional anharmonic terms, whereas here, the quantitative determination of the corresponding parameters shall be addressed. The chosen approach, i.e., the expansion of the self-energy in three variables v_1, v_2, and u up to the sixth-, respectively, eighth-order results in a relatively large number of coupling constants. An explicit calculation is possible only for a few of these parameters, an example of which can be found in Paul *et al.* [28]. Nevertheless, to determine all required parameters, we follow a similar approach as Erba *et al.* [35]. That is, we want to determine the anharmonic couplings by fitting Eq. (3) to a correspondingly large set of DFT calculations. The dataset must be built by various displacements according to the displacement patterns of u, v_1, and v_2. These patterns are obtained from the initial phonon calculation of the previous section. We already reported the patterns for the soft mode, v_1, and v_2 in the previous section. We used these patterns to create structures with different displacements of the atoms by superposition. For the ⟨001⟩ direction, we generated about 2000 of these structures and calculated the corresponding total energies using DFT. This dataset was then used to fit Eq. (4) to determine all coupling parameters. Since we have a large number of parameters to determine, much emphasis was put on the stability of the fit. For that purpose, different fit algorithms like Levenberg-Marquardt, Nelder-Mead, or Powell were used to cross-check the results. Furthermore, a cross-validation procedure was used to investigate the quality of the fit function. A detailed description of the above-mentioned investigations can be found in the Supplemental Material [32]. Concerning the main task, the determination of the coupling parameters, it could be shown that all algorithms yield the same global minimum. The associated calculated parameters are listed in Table S2 [32]. A visualization of the derived potential energy as a function of u_x, v_{1x}, and v_{2x} is provided in Fig. 1(a). It can be observed that the local minima of the potential energy surface are slightly shifted by the inclusion of v_1 and v_2. That means for each $u > 0$ there are associated non-vanishing amplitudes v_1 and v_2, which minimize the energy.

A final necessary step is to incorporate these anharmonic couplings into the effective Hamiltonian. As discussed in Sec. II B, we want to take the relatively simple way here and pack the couplings into adapted k_1 and k_4 parameters. To do this, we evaluate Eq. (4) using the parameters of Table S2 [32] for a discrete range of $u = 0$ to 0.25 Å and simultaneously minimize over the amplitudes v_1 and v_2 [see Fig. 1(b)]. Equation (2a) is then fitted to the data using k_1 and k_4 as fit parameters. The resulting fitted parameters k_1' and k_4' are -1443.850 eV/Å^6 and 17 216.816 eV/Å^8, respectively. A visualization of the self-energy, with and without additional anharmonic couplings, as a function of u in the ⟨001⟩ direction is presented in Fig. 1(c).

Although in this paper we are mainly concerned with the self-energy in the ⟨001⟩ direction, the two other directions, ⟨011⟩ and ⟨111⟩, should also be briefly discussed here. The calculation of the coupling parameters is analogous to the ⟨001⟩ direction, whereby the input structures are generated by displacing atoms in two or three dimensions using the displacement patterns, respectively. The Taylor expansion for these directions can be done in two ways; either one uses vectors $\boldsymbol{u}$, $\boldsymbol{v}_1$, and $\boldsymbol{v}_2$, or one treats each direction individually. The latter is somehow analogous to Eqs. (2a)–(2c) and has the advantage that the series expansion from Eq. (3) can be used. We proceeded with the second approach and also calculated the remaining two directions and the corresponding renormalized total energy. The incorporation of these additional directions into the effective Hamiltonian can be done with a refit using the parameters γ, k_2, and k_3. However, it became apparent that these parameters are only partially capable of properly incorporating the additional information (see Supplemental Material [32] for more details). A solution to overcome this issue is to extend the self-energy from Eq. (2) with additional parameters. For the remainder of this paper, however, we use the parameter set presented above. It should be noted, nevertheless, that this does not leave the other two directions untouched. The incorporation of anharmonic couplings by adjusting k_1 and k_4 also impacts the ⟨011⟩ and ⟨111⟩ directions as one can see in Eqs. (2b) and (2c).

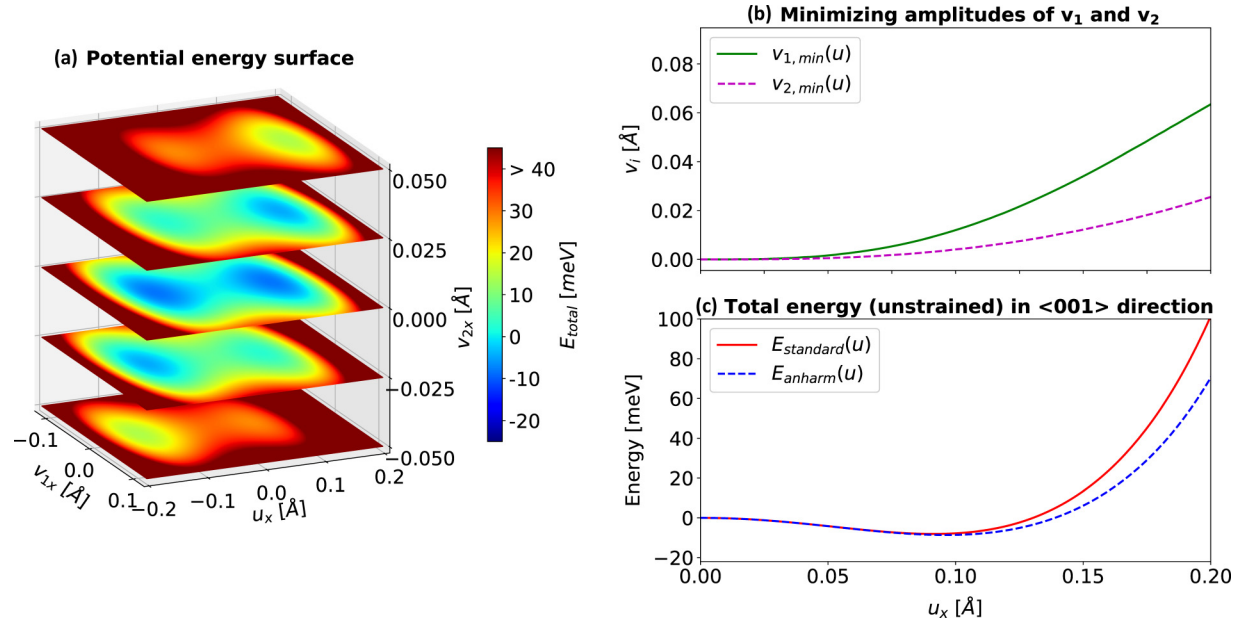

FIG. 1. Visualization of self-energy as a function of the three phonon mode amplitudes u, v_1, and v_2 along the $\langle 001 \rangle$ direction (a). Panel (b) shows the values for v_1 and v_2 that minimize the self-energy for a given u. Panel (c) shows the self-energy back-transformed to a function of one variable u by minimizing the energy with respect to v_1 and v_2 for a given u.

III. METHODOLOGICAL DETAILS

A. Experimental setup

A BT single crystal, polished on both sides, was purchased from SurfaceNet GmbH (48432 Rheine, Germany). Prior to measuring, the sample was held at 353 K for a week in air atmosphere. Electrical contacts were made with silver paint on the top and bottom of the sample ($5 \times 2 \times 0.1$ mm) and the wires connected in—typical for dielectric measurements [43]—a pseudo-four-point configuration. The dielectric data in a frequency range from 20 Hz to 1 MHz were collected with an E4980A Precision *LCR* meter (Agilent). The static hysteresis loops were measured using an AixACCT TF2000 Analyzer combined with a high-voltage booster (HVB 1000) and a Krohn-Hite model 7500 amplifier. For both measurements the temperature (300–540 K) was controlled via a nitrogen flow based cryostat (Novocontrol Quatro Cryosystem).

B. DFT calculations for parametrization of the effective Hamiltonian

For all DFT calculations used for parametrization of the effective Hamiltonian, we applied the projector-augmented [44] DFT package VASP [45–48] and PBEsol [37] as the exchange-correlation functional. All calculations with five-atom unit cells were done using a k grid of size $8 \times 8 \times 8$ and an energy cutoff of 520 eV. The $2 \times 2 \times 2$ supercell calculations were carried out with a k grid of $4 \times 4 \times 4$ and an energy cutoff of 520 eV.

C. MD setup

All MD simulations in the following section were carried out in the NVT ensemble. The Nosé-Poincaré thermostat [49] was used to maintain a constant temperature. For the simulation of the phase diagram, we decided to use a simulation box size of $16 \times 16 \times 16$ unit cells. A comparison with other sizes can be found in the Supplemental Material [32]. A time step of 0.002 ps was used for all simulations. The system was thermalized for 360 ps, and then statistical values were recorded over 40 ps. The phase diagram was obtained using a temperature step of 1 K. The simulation of permittivity as a function of temperature was performed as follows: For each temperature step, which was chosen to be 1 K, the system was thermalized for 2 ns, and then over 2 ns the statistical values were recorded. A simulation box of size $16 \times 16 \times 16$ was also chosen here. The permittivity was calculated using the fluctuations of the dipoles, as shown in Eq. (6). Here, e represents the elementary charge and V the volume of the unit cell.

$$\epsilon_r = \frac{e^2 Z^{*2}}{V k_B \epsilon_0 T} (\langle u^2 \rangle - \langle u \rangle^2). \tag{6}$$

The simulations of polarization–electric field hysteresis curves (P-E loops) were performed for the quasistatic case. An external electric field was applied from −100 to +100 kV/cm in 0.5 kV/cm steps. For each field strength, the system was thermalized over 360 ps, and then the required values were recorded over 40 ps. Here, we chose a simulation box size of $24 \times 24 \times 24$. A comparison to dynamic loops at high frequencies can be found in the Supplemental Material [32]. All simulations were performed using the open-source code FERAM developed by Nishimatsu *et al.* [27,29].

IV. RESULTS

This section will now apply the elaborated parametrization and use it to perform molecular dynamics simulations. At the same time, we performed measurements on BT single crystals to provide a basis for comparison of properties such as dielectric permittivity and ferroelectric hysteresis curves.

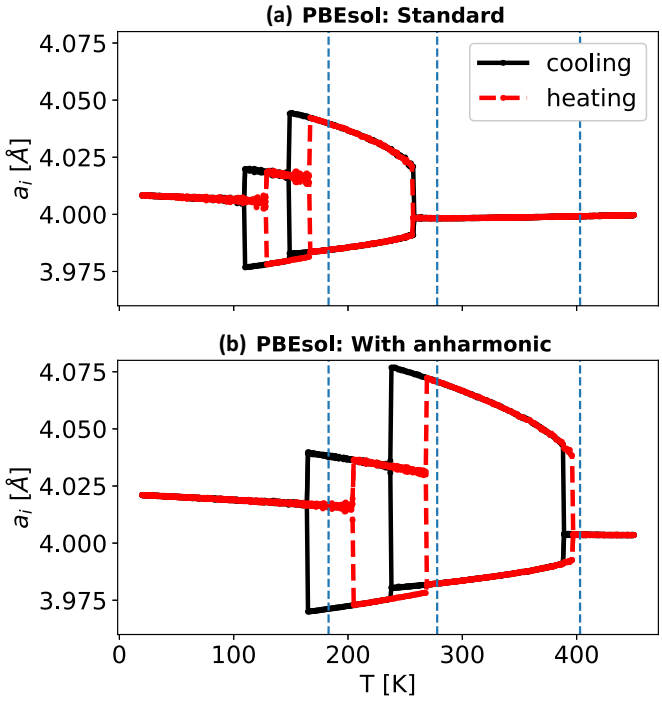

FIG. 2. Phase diagram in terms of the temperature evolution of lattice constants a_i for BT simulated by MD using the two parameter sets (a) without and (b) with additional anharmonic couplings to higher-energy phonons. The black line was obtained by cooling and the red line by heating the system in the MD simulation. The dashed vertical lines represent the experimentally observed transition temperatures.

A. Transition temperatures

First, we consider the simulated phase diagram, i.e., the evolution of the lattice constants as a function of temperature, as shown in Fig. 2. To demonstrate the influence of the additional anharmonic couplings, we also present the result of the conventional Hamiltonian. To account for the effect of hysteresis, heating and cooling simulations were performed in each case, and the transition temperature was taken as the average value between the two. It is obvious that the transition temperatures are significantly closer to the experimental results when additional anharmonic couplings are incorporated. Further, it is observed that the lattice parameters also change accordingly. Thus, an increase of the lattice parameters is observed for all monitored temperatures. The cubic phase shows a lattice constant of 4.00 Å at 405 K in the simulation, which is in excellent agreement with experimental data [50] of 4.00 Å. The lattice parameters of the tetragonal phase, compared with experimental values [50] of $a = 3.99$ Å and $c = 4.04$ Å, are slightly overestimated by the simulation. The same is observed for the lattice parameters [50] of the orthorhombic and rhombohedral phases. For the sake of completeness, thermal expansion should also be briefly discussed here. Although we include a large number of anharmonic terms, the thermal expansion is described qualitatively wrong as shown in Fig. 2. However, these additional couplings are not actively present in our simulation and the original formalism of Nishimatsu *et al.* [29] is used. The latter is known to fail at reproducing the thermal expansion [51]. A solution to this would be to extend the formalism by the degrees of freedom of v_1 and v_2 and to modify the potential of the acoustic mode. However, this is beyond the scope of this paper and may be addressed in a future publication.

Furthermore, we want to compare our simulations with results from the literature. For this purpose, an overview of parametrizations using different exchange-correlation functionals and the corresponding transition temperatures is presented in Table II. The results of the LDA functional show the largest deviation from the experimental data. The application of a constant pressure on top of LDA yields higher temperatures, but rather large deviations are still observed. The WC-GGA functional expectedly gives results similar to our standard PBEsol simulation. SCAN gives similar results. The WC-GGA functional combined with a temperature-dependent external pressure term yields the transition temperature between the cubic and tetragonal phases close to the experimental value. Nevertheless, the best match to experiments is demonstrated by our PBEsol-based scheme with additional anharmonic couplings as well as another flavor for including anharmonic couplings combined with SCAN [28]. The good agreement between simulation and experiment

TABLE II. Comparison of transition temperatures estimated via molecular dynamics simulations based on effective Hamiltonians. The table shows results for different exchange-correlation functionals used in the parametrization of the Hamiltonian. The first set of results is obtained with the conventional Hamiltonian. The second set of results is obtained with applying pressure. The third set of results includes additional anharmonic couplings. R = rhombohedral, O = orthorhombic, T = tetragonal, C = cubic, and Θ = Temperature.

Exchange-correlation functional	Pressure	R↔O		O↔T		T↔C	
LDA [29]	–	95 K	–48%	110 K	–60%	137 K	–66%
WC-GGA [29]	–	102 K	–44%	160 K	–42%	288 K	–29%
SCAN [28]	–	111 K	–39%	141 K	–49%	213 K	–47%
PBEsol (this work)	–	119 K	–35%	158 K	–43%	257 K	–36%
LDA [29]	–5 GPa	210 K	15%	245 K	–12%	320 K	–21%
WC-GGA [29]	–2 GPa	117 K	–36%	218 K	–22%	408 K	1%
WC-GGA [29]	–0.005 Θ GPa	103 K	–44%	187 K	–33%	411 K	2%
SCAN (anharmonic[a]) [28]	–	230 K	26%	278 K	0%	375 K	–7%
PBEsol (this work, anharmonic)	–	186 K	2%	255 K	–8%	395 K	–2%
Expt. [28,52]	–	183 K	0%	278 K	0%	403 K	0%

[a]Different flavor of anharmonic coupling up to second order in v_1 and v_2.

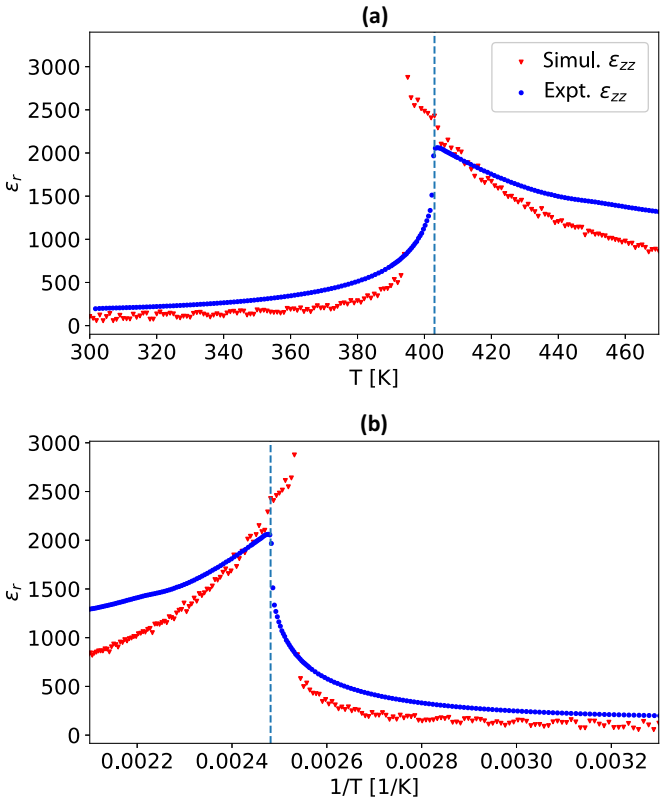

FIG. 3. Permittivity around the cubic to tetragonal phase transition as a function of (a) temperature and (b) inverse temperature, comparing measurements on a BT single crystal (blue) and simulations (red) using the effective Hamiltonian with anharmonic coupling to higher-energy phonons. The dashed line indicates the T_C determined from experiments.

suggests that the local energetic minima are better described by including additional anharmonic couplings. To test this hypothesis, we performed *ab initio* molecular dynamics (AIMD) simulations for different temperatures and compared the potential energy surfaces to those of the effective Hamiltonians. As described in detail in the Supplemental Material [32], the inclusion of anharmonic couplings contributes a significant part to the potential energy surface. Furthermore, the energy differences between AIMD and effective Hamiltonian become smaller when including anharmonic couplings, which indicates that the potential energy surface is better reproduced by the adapted Hamiltonian.

B. Permittivity

The hallmark features of ferroelectric transitions are temperature-dependent peaks in the dielectric permittivity. In Fig. 3, we present the permittivity as a function of temperature around the tetragonal to cubic phase transition measured on a BT single crystal and simulated by MD using the adapted effective Hamiltonian. Similar to the experiment, the results for the simulations were obtained by heating the crystal, i.e., by increasing the temperature in the MD run. The simulated trend of the permittivity below the phase transition shows remarkably good agreement with the experiment. The simulation estimates the maximum permittivity value directly at the phase transition to be 25% higher than the measured one. The value of ϵ_r above T_C is slightly higher in the experiment, whereby even a small peak can be observed at about 450 K. That may be due to an extra relaxation given by impurities present, or slight deviations from perfect stoichiometry, in the single crystal. In summary, the simulation provides good agreement with the measured values. The simulated permittivity for a larger temperature range can be found in the Supplemental Material [32].

C. *P-E* loops

Another essential property of ferroelectric materials represents the system's response to external electric fields, also known as polarization–electric field hysteresis curves (*P-E* loops). In this work, we focus mainly on the temperature range near the phase transition between the paraelectric and ferroelectric phases (i.e., T_C). Already in the 1950s, Merz [53] showed the occurrence of double loops near T_C. Therefore, we decided that this temperature range is ideal for testing our Hamiltonian.

As a starting point, we performed experimental measurements of the *P-E* loops using BT single crystals. The results are shown in Fig. 4(a). At 400 K, just below T_C, we see the typical single-loop ferroelectric hysteresis curve. Just above it, at 406 K, we observe a double loop, but not as pronounced as in Merz's data [53]—this is likely due to the changes in single-crystal growth techniques over the intervening 70 years. At 410 K, finally, the double loop has almost vanished. An explanation for this behavior across T_C can be found in Refs. [53,54].

In the next step, we simulated the *P-E* loops using our effective Hamiltonians. To take into account the slightly lower phase transition temperature found in our simulations, we used the highest temperature that shows pure ferroelectric behavior as reference; i.e., we compare simulations at 397 K to the experiment at 400 K. Subsequently, the temperature for the simulation was increased by the same steps as in the experiment. The results of these simulations are shown in Fig. 4(b). The experiment and simulation show a very good qualitative match, even though our simulation exhibits more pronounced double loops. This is actually in very good agreement with the measurements by Merz [53]. Regarding the saturated polarization, experiment and simulation agree very well, even quantitatively. The corresponding values of the external field in the simulation, however, are about a factor of 5 larger compared to the experimental data.

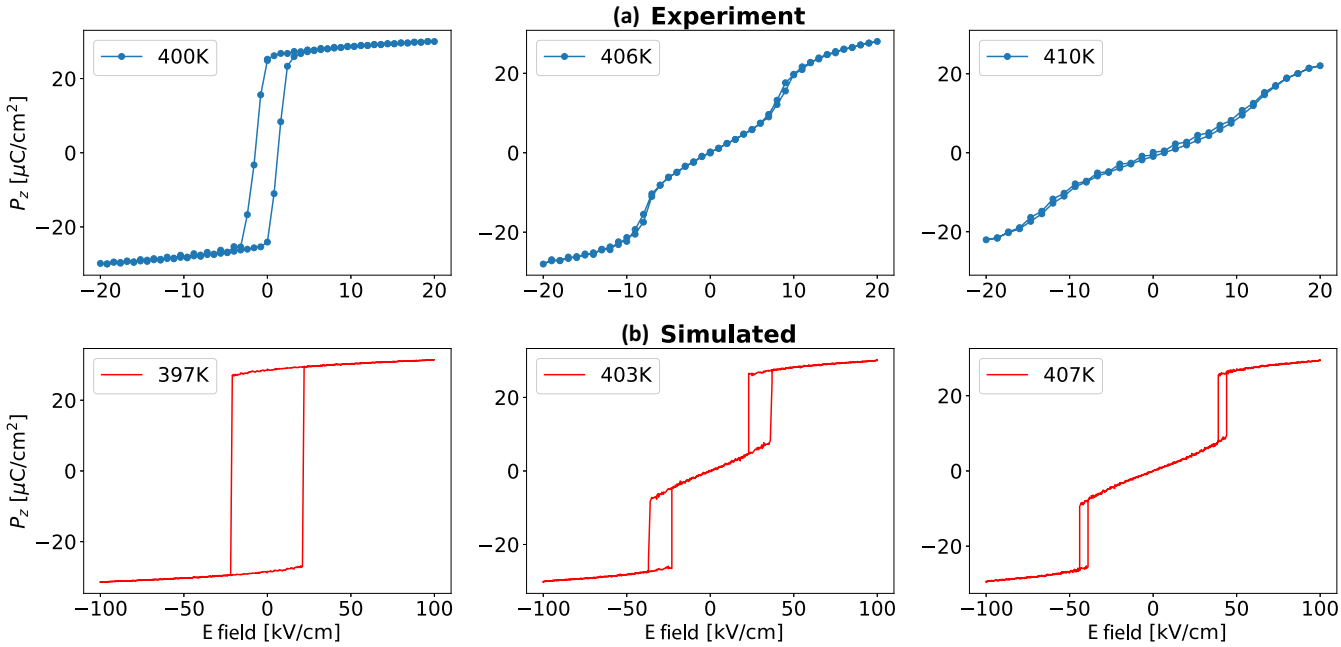

FIG. 4. Comparison between experimental (a) and simulated (b) *P*-*E* loops of BT near the ferroelectric-paraelectric phase transition. The temperatures for the simulated loops were chosen according to the values of the experiment but shifted to the phase transition temperature observed in the simulation.

V. CONCLUSION

In this work, an alternative way to incorporate a variety of anharmonic terms to describe the potential energy surface of BT has been shown. The scheme chosen can be easily applied to other systems and provides a systematic extension of the already established formalism of effective Hamiltonians. Instead of relying on individual anharmonic couplings, a larger number of them is included in this work. By this approach a renormalization of the energy surface is observed, which subsequently contributes to an improved description of the transition temperatures. Another advantage of our scheme is the possible extension to all high-symmetry directions. In this work, we focused exclusively on the ⟨001⟩ direction. Already with this choice the other directions are positively influenced via the chosen parameters and the back-transformation to the original formalism. For further work in this area, the other directions can be taken into account to obtain an even more complete description of the energy surface. Furthermore, the choice of the exchange-correlation functional plays a role. In our case, all calculations were performed with the PBEsol functional. This is obviously a very good choice for the calculation of the required parameters and provides very similar results as the meta-GGA functional SCAN. Comparison with measurements on BT single crystals allowed us to quantify the Hamiltonian as well. The simulated permittivity reflects the measurements very well. The simulation of the hysteresis was carried out for a quasistatic case in order to create a comparison with low-frequency measurements. Thereby, the absolute values of the saturated polarization between simulation and measurement are in good agreement. Also the occurrence of the double hysteresis in the range of the transition temperature T_C can be confirmed by simulation and measurement. Only regarding the values of the external field is there still room for improvement in order to be able to quantify properties such as the energy stored by the system. Altogether, the parameter set presented here provides an excellent basis for further studies and can be used for possible extensions for substituted systems.

ACKNOWLEDGMENTS

This project has received funding from the European Research Council (ERC) under the European Union's Horizon 2020 research and innovation program (Grant Agreement No. 817190). D.M.E. was funded by Deutsche Forschungsgemeinschaft (DFG) Individual Fellowship No. EV 305/1-1. S.K. was supported by the DFG Transregional Research Center TRR80. The computational results presented have been achieved in part using the Vienna Scientific Cluster (VSC).

[1] J. Rödel, K. G. Webber, R. Dittmer, W. Jo, M. Kimura, and D. Damjanovic, J. Eur. Ceram. Soc. **35**, 1659 (2015).

[2] V. Veerapandiyan, F. Benes, T. Gindel, and M. Deluca, Materials (Basel). **13**, 5742 (2020).

[3] D. Xue, P. V. Balachandran, R. Yuan, T. Hu, X. Qian, E. R. Dougherty, and T. Lookman, Proc. Natl. Acad. Sci. **113**, 13301 (2016).

[4] P. V. Balachandran, B. Kowalski, A. Sehirlioglu, and T. Lookman, Nat. Commun. **9**, 1668 (2018).

[5] P. V. Balachandran, A. A. Emery, J. E. Gubernatis, T. Lookman, C. Wolverton, and A. Zunger, Phys. Rev. Materials **2**, 043802 (2018).

[6] R. Yuan, Z. Liu, P. V. Balachandran, D. Xue, Y. Zhou, X. Ding, J. Sun, D. Xue, T. Lookman, Adv. Mater. **30**, 1702884 (2018).

[7] L. Bellaiche, A. García, and D. Vanderbilt, Ferroelectrics **266**, 41 (2002).
[8] J. Íñiguez and L. Bellaiche, Phys. Rev. Lett. **87**, 095503 (2001).
[9] C. Mentzer, S. Lisenkov, Z. G. Fthenakis, and I. Ponomareva, Phys. Rev. B **99**, 064111 (2019).
[10] M. Acosta, N. Novak, V. Rojas, S. Patel, R. Vaish, J. Koruza, G. A. Rossetti, and J. Rödel, Appl. Phys. Rev. **4**, 041305 (2017).
[11] G. Wang, Z. Lu, Y. Li, L. Li, H. Ji, A. Feteira, D. Zhou, D. Wang, S. Zhang, and I. M. Reaney, Chem. Rev. **121**, 6124 (2021).
[12] T. Maiti, R. Guo, and A. S. Bhalla, Appl. Phys. Lett. **90**, 182901 (2007).
[13] M. Valant, Prog. Mater. Sci. **57**, 980 (2012).
[14] A. J. Moulson and J. M. Herbert, *Electroceramics: Materials, Properties, Applications*, 2nd ed. (John Wiley & Sons Ltd., New York, 2003).
[15] H. D. Megaw, Acta Crystallogr. **5**, 739 (1952).
[16] R. D. King-Smith and D. Vanderbilt, Ferroelectrics **136**, 85 (1992).
[17] R. E. Cohen and H. Krakauer, Phys. Rev. B **42**, 6416 (1990).
[18] W. Zhong, D. Vanderbilt, and K. M. Rabe, Phys. Rev. B **52**, 6301 (1995).
[19] J. C. Wojdeł, P. Hermet, M. P. Ljungberg, P. Ghosez, and J. Íñiguez, J. Phys.: Condens. Matter **25**, 305401 (2013).
[20] J. M. Vielma and G. Schneider, J. Appl. Phys. **114**, 174108 (2013).
[21] R. Pirc and R. Blinc, Phys. Rev. B **60**, 13470 (1999).
[22] L.-Q. Chen, J. Am. Ceram. Soc. **91**, 1835 (2008).
[23] A. F. Devonshire, London, Edinburgh, Dublin Philos. Mag. J. Sci. **40**, 1040 (1949).
[24] A. F. Devonshire, London, Edinburgh, Dublin Philos. Mag. J. Sci. **42**, 1065 (1951).
[25] R. D. King-Smith and D. Vanderbilt, Phys. Rev. B **49**, 5828 (1994).
[26] U. V. Waghmare and K. M. Rabe, Phys. Rev. B **55**, 6161 (1997).
[27] T. Nishimatsu, U. V. Waghmare, Y. Kawazoe, and D. Vanderbilt, Phys. Rev. B **78**, 104104 (2008).
[28] A. Paul, J. Sun, J. P. Perdew, and U. V. Waghmare, Phys. Rev. B **95**, 054111 (2017).
[29] T. Nishimatsu, M. Iwamoto, Y. Kawazoe, and U. V. Waghmare, Phys. Rev. B **82**, 134106 (2010).
[30] K. M. Rabe and U. V. Waghmare, Phys. Rev. B **52**, 13236 (1995).
[31] J. H. Lee, U. V. Waghmare, and J. Yu, J. Appl. Phys. **103**, 124106 (2008).
[32] See Supplemental Material at http://link.aps.org/supplemental/10.1103/PhysRevB.106.064108 for derivation of full fitting function, strain-phonon coupling, and stability of fit.
[33] H. T. Stokes, D. M. Hatch, and B. J. Campbell, INVARIANTS, ISOTROPY Software Suite, iso.byu.edu
[34] D. M. Hatch and H. T. Stokes, J. Appl. Crystallogr. **36**, 951 (2003).
[35] A. Erba, J. Maul, M. Ferrabone, P. Carbonnière, M. Rérat, and R. Dovesi, J. Chem. Theory Comput. **15**, 3755 (2019).
[36] J. A. Nelder and R. Mead, Comput. J. **7**, 308 (1965).
[37] G. I. Csonka, J. P. Perdew, A. Ruzsinszky, P. H. T. Philipsen, S. Lebègue, J. Paier, O. A. Vydrov, and J. G. Ángyán, Phys. Rev. B **79**, 155107 (2009).
[38] S. Piskunov, E. Heifets, R. I. Eglitis, and G. Borstel, Comput. Mater. Sci. **29**, 165 (2004).
[39] R. A. Evarestov, Phys. Rev. B **83**, 014105 (2011).
[40] R. Wahl, D. Vogtenhuber, and G. Kresse, Phys. Rev. B **78**, 104116 (2008).
[41] Z. Wu and R. E. Cohen, Phys. Rev. B **73**, 235116 (2006).
[42] J. Sun, A. Ruzsinszky, and J. P. Perdew, Phys. Rev. Lett. **115**, 036402 (2015).
[43] P. Lunkenheimer, S. Krohns, S. Riegg, S. G. Ebbinghaus, A. Reller, and A. Loidl, Eur. Phys. J.: Spec. Top. **180**, 61 (2009).
[44] P. E. Blöchl, Phys. Rev. B **50**, 17953 (1994).
[45] G. Kresse and D. Joubert, Phys. Rev. B **59**, 1758 (1999).
[46] G. Kresse and J. Furthmüller, Phys. Rev. B **54**, 11169 (1996).
[47] G. Kresse and J. Furthmüller, Comput. Mater. Sci. **6**, 15 (1996).
[48] G. Kresse and J. Hafner, Phys. Rev. B **49**, 14251 (1994).
[49] S. D. Bond, B. J. Leimkuhler, and B. B. Laird, J. Comput. Phys. **151**, 114 (1999).
[50] S. F. Yuk, K. C. Pitike, S. M. Nakhmanson, M. Eisenbach, Y. W. Li, and V. R. Cooper, Sci. Rep. **7**, 43482 (2017).
[51] S. Tinte, J. Íñiguez, K. M. Rabe, and D. Vanderbilt, Phys. Rev. B **67**, 064106 (2003).
[52] C. J. Johnson, Appl. Phys. Lett. **7**, 221 (1965).
[53] W. J. Merz, Phys. Rev. **91**, 513 (1953).
[54] L. E. Cross, J. Phys. Soc. Jpn. **23**, 77 (1967).